EDGE ARTICLE

Check for updates

High-efficiency non-doped near-ultraviolet OLEDs achieved by regulating excited-state spatial distribution through molecular optimization to realize hybridized local and charge-transfer (HLCT) characteristics

Daokun Zhong,[ab] Ruiqin Zhu,[a] Jie Zhang,[b] Peng Tao, [ID][b] Bochao Su, [ID][a] Xiaolong Yang, [ID][a] Yuanhui Sun, [ID][a] Ling Yue, [ID][a] Guijiang Zhou [ID] *[a] and Wai-Yeung Wong [ID] *[b]

The development of high-performance near-ultraviolet organic light-emitting diodes (NUV-OLEDs) remains challenging due to their intrinsic wide-bandgap characteristics. Therefore, this study fully exploits the weak electron-accepting characteristics of the PPI group, combined with its high photoluminescence quantum yield (PLQY) and excellent thermal stability. Through a precise molecular structure modulation strategy involving direct introduction of electron-donating diphenylamine groups into the side phenyl ring and systematic integration of donor/acceptor units with tailored electronic properties into the main backbone, effective control of excited-state characteristics and their spatial distribution was successfully achieved. Based on this molecular design concept, four near-ultraviolet luminescent molecules (TPA-PPI, DTPA-PPI, TPAAd-PPI, and TPA-POPPI) with hot-exciton properties were successfully developed, significantly improving the material's PLQY and electroluminescence (EL) performance. Notably, compared to analogous structures, the TPAAd-PPI derivatives demonstrate significantly enhanced PLQY and EL performance. Specifically, the external quantum efficiency (EQE) was substantially improved from 4.0% for DMP to 12.1%, while the CIE_y coordinates decreased from 0.053 to 0.048, achieving near-ultraviolet emission. Remarkably, the non-doped device based on TPA-POPPI achieved a record-high EQE of 13.8%. These outstanding results underscore the significant potential of this innovative molecular design strategy for developing high-performance NUV-OLEDs.

1 Introduction

In recent years, organic light-emitting diodes (OLEDs) have achieved large-scale commercialization and rapidly emerged as one of the most promising next-generation display technologies in fields such as televisions, smartphones, automotive displays, laptops, and wearable devices, owing to their low power consumption, fast response, wide viewing angles, transparency, and flexible bendability.[1–4] Thanks to the persistent research efforts by numerous OLED researchers dedicated to developing high-performance red, green, and blue materials for display and lighting applications, significant progress has been achieved in fluorescent materials, phosphorescent materials, thermally activated delayed fluorescence (TADF) materials, as well as

[a]Engineering Research Center of Energy Storage Materials and Devices, School of Chemistry, State Key Laboratory for Mechanical Behavior of Materials, Xi'an Jiaotong University, Xi'an 710049, P. R. China. E-mail: zhougj@mail.xjtu.edu.cn

[b]Department of Applied Biology and Chemical Technology, The Hong Kong Polytechnic University, Hung Hom, Hong Kong, China. E-mail: wai-yeung.wong@polyu.edu.hk

hybrid localized and charge-transfer (HLCT) OLED materials featuring high-order reverse inter-system crossing (hRISC) characteristics.[3,5,6] Recently, near-ultraviolet (NUV) OLEDs have attracted growing attention due to their potential applications in sterilization, high-density information storage, and sensing technologies. However, the development of highly efficient near-ultraviolet (NUV) luminescent materials remains challenging due to the substantial band-gap energy of NUV-emitting molecules, which complicates their molecular design.[7,8]

Rational modulation of excited-state properties represents a crucial strategy for achieving high-efficiency NUV emission. During photophysical processes, electrostatic coulombic interactions between electrons and holes lead to the formation of two distinct types of excited states exhibiting either locally excited (LE) or charge-transfer (CT) characteristics. The LE state, characterized by highly localized electron cloud distribution, facilitates efficient radiative transitions, thereby exhibiting high photoluminescence quantum yield (PLQY) and short-wavelength emission characteristics.[9] However, pure LE-state materials possess an inherent limitation, and their restricted

triplet-to-singlet exciton conversion efficiency fundamentally constrains device exciton utilization.[10–15] In contrast, weakly bound CT states (as exemplified by classical donor–acceptor (D–A) type TADF materials) demonstrate distinct advantages in electroluminescent processes. Nevertheless, in CT state materials, the minimal orbital overlap during electron transitions significantly suppresses radiative decay efficiency, severely compromising PLQY.[9] In contrast, the HLCT mechanism, through synergistic modulation of LE and CT state characteristics, enables simultaneous achievement of high exciton utilization efficiency (EUE) and superior PLQY, thereby offering an effective solution for developing high-performance NUV materials.[11,16–18]

The 1,2-diphenyl-phenanthroimidazole (PPI) group is widely used in the design of high-efficiency HLCT materials due to its weak electron-accepting ability, high PLQY and good thermal stability.[6,19,20] Ma and co-workers pioneered the incorporation of PPI and its derivatives into HLCT materials, achieving outstanding electroluminescent performance.[21,22] This groundbreaking work has attracted extensive attention and prompted in-depth exploration by researchers. As shown in Fig. 1a, previous studies have primarily focused on modifying the PPI main backbone structure and extending the conjugation length to regulate the excited-state properties of the material.[23–26] For instance, Xue and co-workers designed and synthesized two D–π–A-type deep-blue emitters (CZFPI and TPAFPI) using fluorene as the π-bridge with carbazole and triphenylamine derivatives serving as D units.[27] The results demonstrate that the incorporation of the π-bridge effectively modulates the relative contributions of the LE and CT states, leading to highly efficient EL performance. Additionally, Vinich's team successfully achieved HLCT characteristics with a PLQY approaching 100% by employing azine-based compounds as the A units and linking them to a PPI group *via* a π-bridge.[28] By extending the π-conjugated system along the molecular backbone and introducing D or A units, the ratio of LE and CT states can be effectively modulated, thereby achieving high PLQY and electroluminescence (EL) performance. However, excessive π-conjugation leads to an emission red-shift, making NUV emission difficult to achieve.[29]

Based on the aforementioned considerations, as illustrated in Fig. 1, this study employs a PPI group as the core structural unit. By introducing diphenylamine as D units on the molecular side phenyl ring, a classic D–A molecular architecture was constructed. This design not only optimizes optoelectronic performance by steering the transition direction of the CT state but also significantly enhances hole injection/transport capabilities. Simultaneously, it shortens the π-conjugation length and localizes the LE character predominantly on the PPI group (Fig. 2). Fig. 2 shows that incorporation of different D or A groups systematically transfers LE and CT state distributions from the side phenyl ring to the PPI main backbone, except in TPAAd-PPI. This structural evolution will effectively enhance EUE, thereby improving the EL performance while suppressing emission red-shift to achieve NUV emission. Guided by this molecular design strategy, four HLCT emitters (TPA-PPI, DTPA-PPI, TPAAd-PPI, and TPA-POPPI) were successfully synthesized. Comprehensive experimental characterization and theoretical calculations demonstrate that systematic molecular optimization progressively enhanced the photoluminescence quantum yield from 65% (TPA-PPI) to 87% (TPA-POPPI). Remarkably, the optimized TPA-POPPI emitter achieved an outstanding 13.8% EQE in non-doped devices while maintaining NUV characteristics (CIE$_y$ = 0.054). These encouraging results demonstrate that molecular-level control of excited-state properties can simultaneously enhance PLQY and EQE while achieving NUV characteristics.

2 Results and discussion

2.1. Molecular synthesis, characterization and thermal properties

The synthetic strategies for both intermediate and target compounds are outlined in Scheme S1, with detailed synthetic procedures provided in the SI. After purification by column chromatography and recrystallization, the target material was characterized by ^{1}H NMR, ^{13}C NMR and high resolution mass spectrometry. The detailed procedures and structural characterization data are given in the SI. Additionally, the thermal properties of TPA-PPI, DTPA-PPI, TPAAd-PPI and TPA-POPPI were investigated through thermogravimetric analysis (TGA) under a nitrogen flow. The TGA results revealed their high thermal stability, with decomposition temperatures all exceeding 410 °C (Fig. S1). The good thermal stability of these four HLCT emitters ensures stability during the fabrication and operation of the respective EL devices.

2.2. Theoretical calculations

To gain insight into the molecular geometries and electronic properties, density functional density (DFT) and time dependent DFT (TD-DFT) calculations in a vacuum were performed using Gaussian 09 software at the B3LYP/6-31G (d,p) level. As shown in Fig. 2, for TPA-PPI, the dihedral angle between the phenyl ring on the PPI group side phenyl ring and the PPI core structure is 80.11°, approaching a perpendicular orientation. Such a large dihedral angle configuration facilitates the
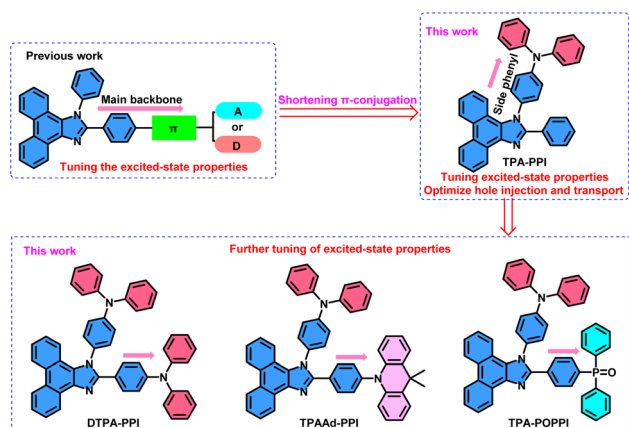

Fig. 1 Molecular design strategy and structural characteristics.
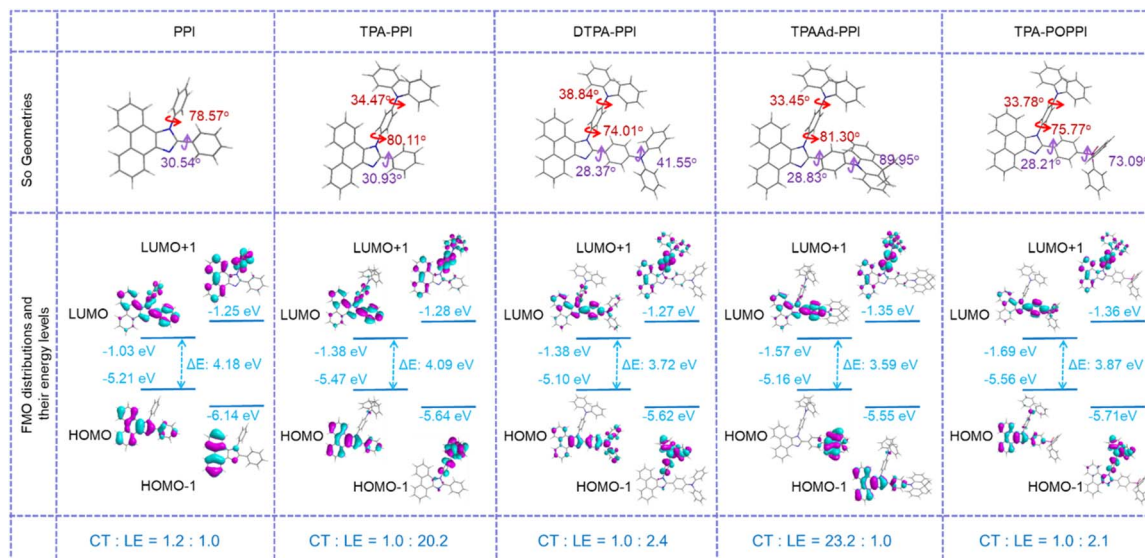
Fig. 2 Molecular geometries in the ground state, FMO distributions and calculated energy levels and the ratio of CT and LE states of PPI, TPA–PPI, DTPA–PPI, TPAAd–PPI and TPA-POPPI.

formation of the CT state. The highest occupied molecular orbital (HOMO) is primarily localized on the PPI group and does not extend to the side phenyl ring. In contrast, the lowest unoccupied molecular orbital (LUMO) is mainly distributed around the two phenyl rings and two nitrogen atoms of the PPI group, resulting in effective orbital overlap at the carbon-linked phenyl rings of the PPI unit. Based on the combined HOMO and LUMO distributions, TPA-PPI exhibits significant CT and LE transition processes. However, the high proportion of the LE state (CT : LE = 1.0 : 20.4) limits the triplet-to-singlet exciton conversion efficiency, thereby restricting the upper limit of luminescence efficiency. Notably, compared to PPI, TPA-PPI exhibits no significant changes in the HOMO and LUMO distributions, but its LUMO energy level decreases substantially from 1.02 eV to 1.38 eV. These results indicate that introducing a diphenylamine group onto the side phenyl ring of PPI facilitates improved electron injection in devices.

Compared to the TPA-PPI molecule, the dihedral angle between the phenyl ring on the main backbone and the PPI core in DTPA-PPI decreases from 30.93° to 28.37°. This structural change effectively promotes the formation of the LE state by reducing steric hindrance. In the DTPA-PPI molecule, the HOMO is primarily distributed over the PPI core and the diphenylamine groups connected to the main backbone phenyl ring, while the LUMO is mainly localized around the main backbone phenyl ring and the two nitrogen atoms of the PPI unit, forming significant orbital overlap in the main backbone phenyl ring region of the PPI core. This electronic structure indicates the coexistence of distinct CT and LE transition processes. Notably, compared to TPA-PPI, the LUMO distribution on the branched phenyl rings of DTPA-PPI is significantly reduced, demonstrating that introducing diphenylamine groups into the main backbone effectively shifts the CT state toward the PPI core region of the main backbone. This results in

a relatively balanced ratio between the CT and LE states (CT : LE = 1.0 : 2.4) during the transition process of the DTPA-PPI molecule, enabling full utilization of the triplet-to-singlet exciton conversion efficiency and consequently enhancing the PLQY. When the diphenylamine group on the main backbone was replaced with the stronger electron-donating 9,9-dimethyl-9,10-dihydroacridine (Ad), the torsion angle between the Ad group and the PPI main-chain phenyl ring in TPAAd-PPI significantly increased to 89.95°. This substantial molecular distortion, combined with the strong electron-donating capability of the Ad group, endows the molecule with distinct CT state characteristics. Notably, in TPAAd-PPI, the HOMO is completely localized on the Ad group, while the LUMO is primarily distributed around the PPI main backbone phenyl ring and the two nitrogen atoms, resulting in complete spatial separation between the HOMO and LUMO. This orbital separation leads to the absence of an LE state, consequently reducing the radiative transition efficiency and ultimately adversely affecting the PLQY of the molecule. Consequently, the introduction of stronger electron-donating D groups was discontinued, and instead the electron-accepting diphenylphosphine oxide group was incorporated into the PPI main backbone. Structural analysis revealed a torsional angle of 73.09° between this group and the main backbone phenyl ring. This substantial torsional angle induces significant separation of molecular orbitals, with the HOMO primarily localized on the PPI group and the LUMO concentrated on both the phenyl ring and phosphorus atom of the PPI main backbone. This electronic distribution characteristic confirms the coexistence of prominent CT and LE states in TPA-POPPI, with the LE state being concentrated towards the PPI core. Thus, a balanced ratio of CT to LE states (CT : LE = 1.0 : 2.1) similar to that of DTPA-PPI is formed, which is conducive to improving the luminescence efficiency.

To further investigate their excited-state characteristics, a systematic analysis of the natural transition orbitals (NTOs) was performed for these four compounds. Fig. 3 displays selected major NTOs along with the energy levels of the first ten

singlet (S_1–S_{10}) and triplet (T_1–T_{10}) states, while Fig. S2–S9 provide detailed NTO results based on S_1–S_{10} and T_1–T_{10}. First, the calculated energy level difference ($\Delta E_{S_1-T_1}$) between the T_1 and S_1 states was determined to be as high as 0.983, 0.746, 0.357
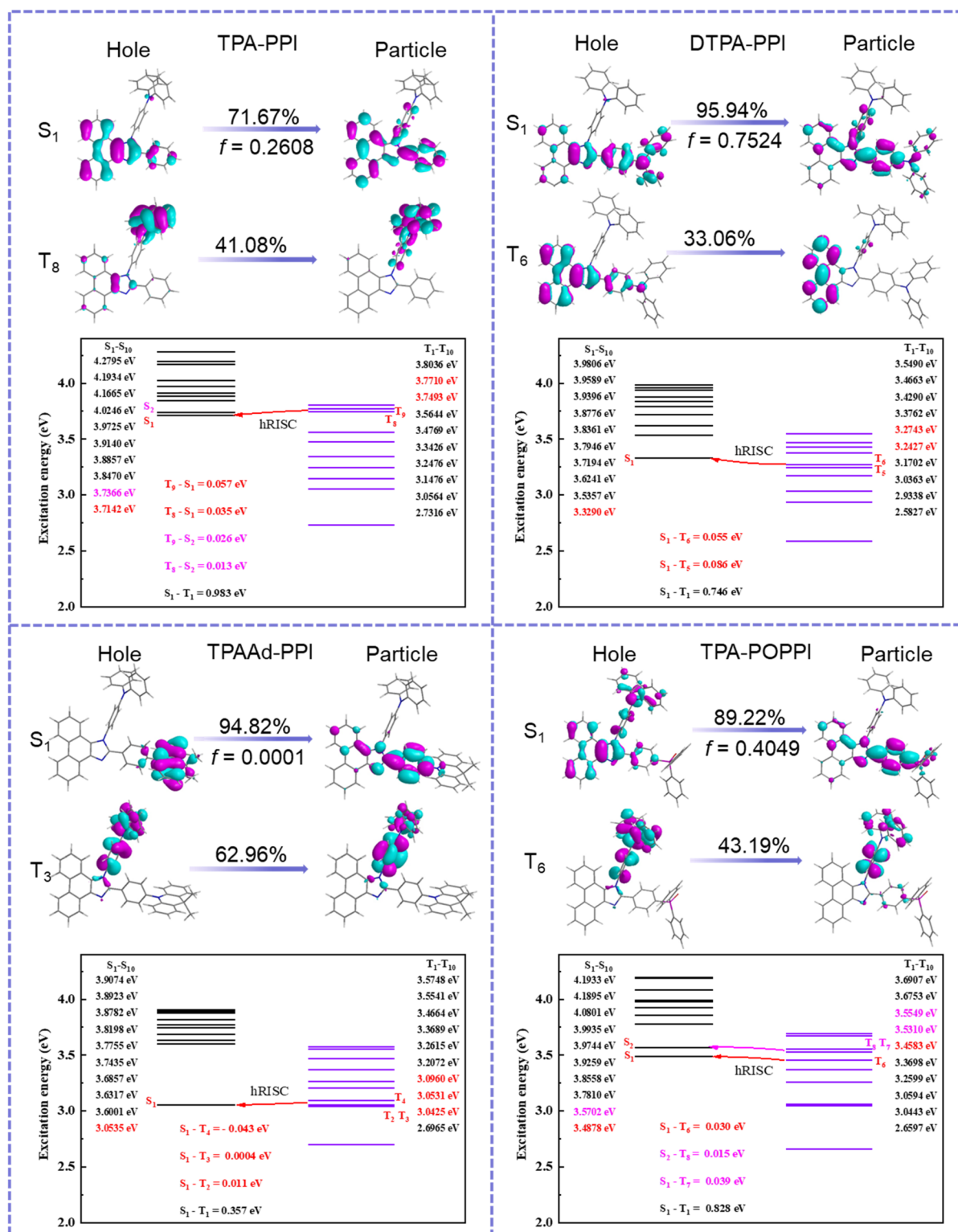

Fig. 3 The natural transition orbitals and the energy levels of the first ten singlet and triplet states of TPA-PPI, DTPA-PPI, TPAAd-PPI and TPA-POP.

and 0.828 eV for TPA-PPI, DTPA-PPI, TPAAd-PPI and TPA-POPPI, respectively (Fig. 3). The relatively large ΔE_{S1-T1} inhibits the reverse intersystem crossing (RISC) process from $T_1 \rightarrow S_1$, thereby preventing these four compound systems from exhibiting thermally activated delayed fluorescence (TADF) characteristics. Secondly, as shown in Fig. 3, the hole-particle analysis of the S_1 state reveals that the TPA-PPI and DTPA-PPI systems exhibit HLCT characteristics dominated by the LE state, whereas the TPAAd-PPI and TPA-POPPI systems demonstrate HLCT properties primarily governed by the CT state. This finding confirms that introducing donor and acceptor moieties with varying electron-donating and -withdrawing capabilities onto the PPI backbone can effectively modulate the composition ratio between CT and LE states in these molecular systems. Further systematic analysis of the first ten singlet and triplet energy levels reveals that the energy gaps between specific states are consistently below 0.1 eV (S_1/S_2 and T_8/T_9 for TPA-PPI, S_1 and T_5/T_6 for DTPA-PPI, S_1 and $T_2/T_3/T_9$ for TPAAd-PPI, and S_1–T_6 and S_2–T_7/T_8 for TPA-POPPI, Fig. S2–S9) Notably, the natural transition orbitals (NTOs) of these higher-lying triplet states (T_n, $n > 1$) exhibit mixed CT and LE characteristics. This finding demonstrates that all four molecular systems can achieve efficient energy conversion through high-lying reverse intersystem crossing (hRISC), thereby providing additional evidence for their HLCT nature.

2.3. Photophysical properties

To investigate the photophysical properties of these four compounds in the monomeric state, we measured their ultraviolet-visible (UV-vis) absorption and photoluminescence (PL) spectra in dilute solutions (10^{-5} M) using solvents of varying polarity (detailed data are provided in Tables S2–S5). As shown in Fig. 4a, all four molecules exhibit two distinct absorption peaks. The absorption peak located in the range of 285–310 nm can be attributed to the $\pi \rightarrow \pi^*$ electronic transition based on the PPI structure. It is noteworthy that TPA-PPI, TPAAd-PPI, and TPA-POPPI all display a similar absorption band at around 365 nm. According to the HOMO and LUMO localization analysis depicted in Fig. 2, this absorption feature can be primarily ascribed to intramolecular charge transfer (ICT), with a secondary contribution from the π–π^* transition of the PPI unit. In contrast, the absorption band of DTPA-PPI at around 365 nm is predominantly characterized by the π–π^* transition of the PPI unit, with a secondary contribution from the CT along the backbone direction from diphenylamine to the PPI moiety.

The PL spectra (Fig. 4b) of all four molecules in hexane solution exhibit distinct vibrational fine structures and NUV emission peaks, indicating that their emission primarily originates from a LE state-dominated process. Notably, the vibrational fine structures of these molecules gradually diminish with increasing solvent polarity, a phenomenon that correlates well with their progressively enlarged Stokes shifts. Particularly, this evolution trend shows strong dependence on the introduced electron-donating groups (including diphenylamine with varied donor strengths, Ad groups, and diphenylphosphine oxide moieties). These results demonstrate that incorporating these functional groups can effectively modulate the relative contribution of CT states in the molecular systems. The enhanced contribution of CT states facilitates the $T_n \rightarrow S_1$ ($n > 1$) transition efficiency, thereby improving the EUE of the
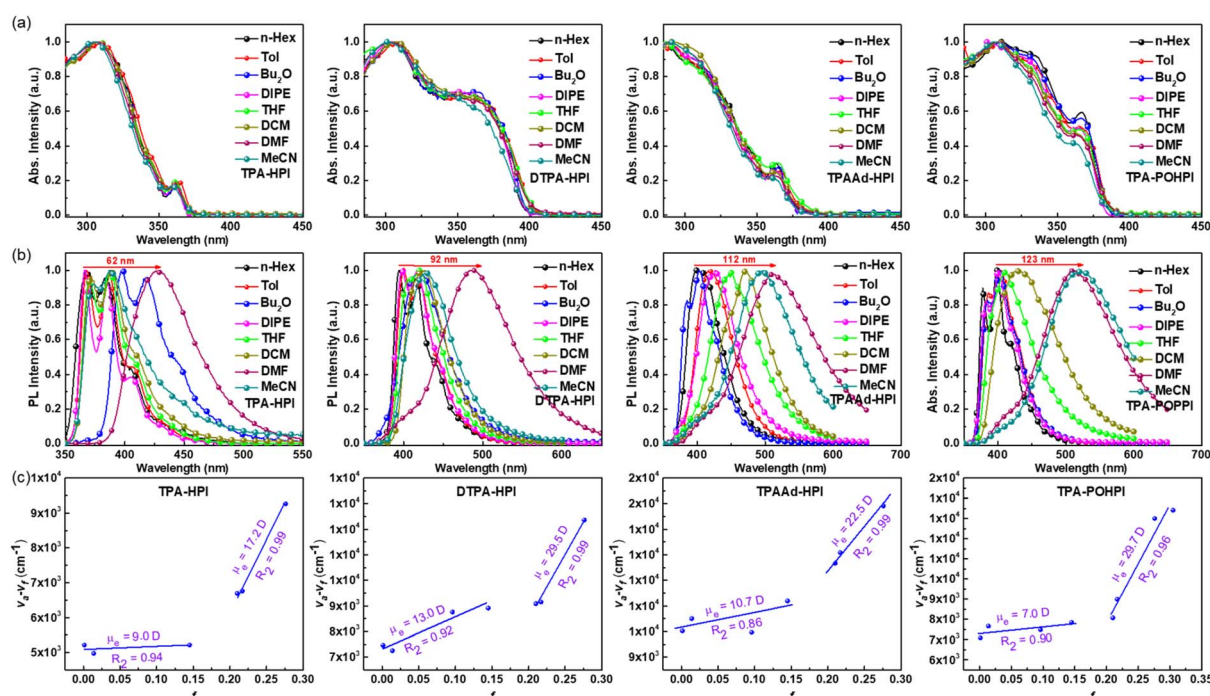

Fig. 4 The UV-vis absorption (a) and PL spectra (b) in dilute solutions (10^{-5} M) using solvents of varying polarity and solvatochromic Lippert–Mataga models with the Stokes shifts (c) for TPA-PPI, DTPA-PPI, TPAAd-PPI and TPA-POPPI.

molecules. This results in a marked improvement in PLQY, with TPA-PPI demonstrating a PLQY of 0.65 in toluene (Table S1), while DTPA-PPI, TPAAd-PPI, and TPA-POPPI achieve enhanced values of 0.83, 0.81, and 0.87, respectively. To further reveal their excited state properties, the corresponding Lippert–Mataga solvatochromic models of the four materials further reveal their distinct excited state properties, as shown in Fig. 4c. In low-polarity solvents, these four molecules exhibit excited-state dipole (μ_e) moments of 9.0 D, 13.0 D, 10.7 D, and 7.0 D, respectively. The relatively small μ_e values indicate that their emission in low-polarity solvents primarily originates from radiative transitions of the LE state. In strongly polar solvents, the μ_e of TPA-PPI, DTPA-PPI, TPAAd-PPI, and TPA-POPPI increases significantly to 17.2 D, 29.5 D, 22.5 D, and 29.7 D, respectively. This observation clearly demonstrates that the emission mechanism in such solvent environments primarily originates from radiative transitions of the CT excited state. More importantly, these data directly confirm that all four molecules exhibit HLCT characteristics. Furthermore, the significantly higher μ_e values of DTPA-PPI, TPAAd-PPI, and TPA-POPPI compared to TPA-PPI in strongly polar solvents demonstrate that introducing donor or acceptor groups into the PPI backbone can effectively modulate and enhance the contribution ratio of the molecular CT state.

In addition to TPA-PPI, the other three molecules exhibit a significant disappearance of the fine structure in their PL spectra when incorporated into poly(methyl methacrylate) (PMMA) films (Fig. S10), along with a notable redshift compared to their solution state. This phenomenon indicates the presence of significant intermolecular aggregation in these molecules within the solid-state films. According to the fluorescence and phosphorescence spectral measurements, the ΔE_{S1-T1} between the S_1 and T_1 states of these four molecules is 0.26, 0.40, 0.32 and 0.25 eV (Table S1), respectively. Such large energy gaps significantly hinder the RISC process from $T_1 \rightarrow S_1$, making it difficult for these molecules to exhibit TADF characteristics. Meanwhile, the transient photoluminescence decay curves of these doped films reveal that all molecules exhibit a bi-exponential decay feature, comprising a fast decay component with lifetimes ranging from 1.3 to 5.4 ns and a long-lived component with lifetimes between 4.3 and 10.6 ns (Fig. S10). The former can be attributed to prompt fluorescence emanating from singlet excitons, whereas the latter can be identified as delayed fluorescence resulting from hRISC processes, which converts triplet excitons into singlet excitons. The gradual decrease in delayed luminescence lifetime demonstrates that introducing donor or acceptor moieties into the PPI main backbone can modulate the proportion of CT states, thereby effectively enhancing the hRISC rate and further improving the PLQY. Based on this, the PLQY of TPA-PPI in PMMA is 0.61 (Table S1), while those of DTPA-PPI, TPAAd-PPI, and TPA-POPPI increase to 0.79, 0.75, and 0.82, respectively.

2.4. Electrochemical properties

The electrochemical properties of these NUV emitters were characterized by cyclic voltammetry (CV) in degassed acetonitrile using ferrocene as the internal standard (Table S6 and Fig. S11). As shown in Fig. S10 and Table S6, all molecules exhibit three oxidation processes attributable to oxidation of both the PPI core and donor groups. TPA-PPI displays a first oxidation potential of 0.62 V. Incorporation of diphenylamine groups into the PPI main backbone reduces the first oxidation potential to 0.49 V in DTPA-PPI. Introduction of the more electron-donating Ad group further decreases the oxidation potential to 0.48 V in TPAAd-PPI, demonstrating enhanced hole injection capability. For TPA-POPPI, the introduction of electron-withdrawing diphenylphosphine oxide groups on the PPI main backbone yields a first oxidation potential of 0.59 V, which remains lower than that of TPA-PPI (0.62 V), confirming maintained hole injection improvement. Notably, the diphenylphosphine oxide moiety simultaneously enhances both hole injection and charge transport properties. These systematic oxidation potential variations demonstrate that strategic incorporation of D or A groups on the PPI backbone effectively modulates and enhances the materials' EL performance.

2.5. EL performance

Inspired by their excellent performance in potential hRISC channels and outstanding bipolar transport characteristics, the electroluminescent properties of TPA-PPI, DTPA-PPI, TPAAd-PPI, and TPA-POPPI in non-doped OLEDs were further investigated. The device structure was ITO/HATCN (5 nm)/TPAC (25 nm)/TCTA (15 nm)/emissive layer (20 nm)/TmPyPb (40 nm)/LiF (1 nm)/Al (100 nm)in which indium tin oxide (ITO) and aluminum (Al) serve as the anode and cathode; hexaazatriphenylenehexacarbonitrile (HATCN) and lithium fluoride (LiF) function as the hole- and electron-injection layers; tris(4-carbazoyl-9-ylphenyl)amine (TCTA) serves as an exciton blocking layer; di-(4-(N,N-ditolyl-amino)-phenyl)cyclohexane (TAPC) and 1,3,5-tri[(3-pyridyl)-phen-3-yl]benzene (TmPyPb) function as the hole and electron-transport layers, respectively. The energy level alignment and chemical structure of the materials used in the OLEDs are shown Fig. 5. The EL performances of non-doped devices are also shown in Fig. 5 and summarized in Table 1.

All the non-doped devices (A–D) with TPA-PPI, DTPA-PPI, TPAAd-PPI and TPA-POPPI as emitters exhibit turn-on voltages of 3.0–3.1 V (Fig. 5 and Table 1), close to the E_g value (Table S6), indicating effective charge carrier injection, transport, and recombination in these devices. This can be attributed to the bipolar transport capability of the emitters. The maximum luminance values of 2506.4, 4536.5, 47 115.8 and 5687.7 cd m^{-2} are achieved in the devices A, B, C and D, respectively. Notably, the EL efficiency of device A is significantly lower than that of the other three devices. This is because the D or A groups introduced into the main backbone of the other three emitters effectively modulate their excited-state properties, thereby enhancing and balancing charge carrier injection and transport. The device D based on TPA-POPPI achieves the most outstanding EL performance with an EQE$_{max}$ value of 13.8%, while the EQE$_{max}$ values of the devices A, B and C based on TPA-PPI, DTPA-PPI and TPAAd-PPI are 5.6%, 12.1% and 11.6%,
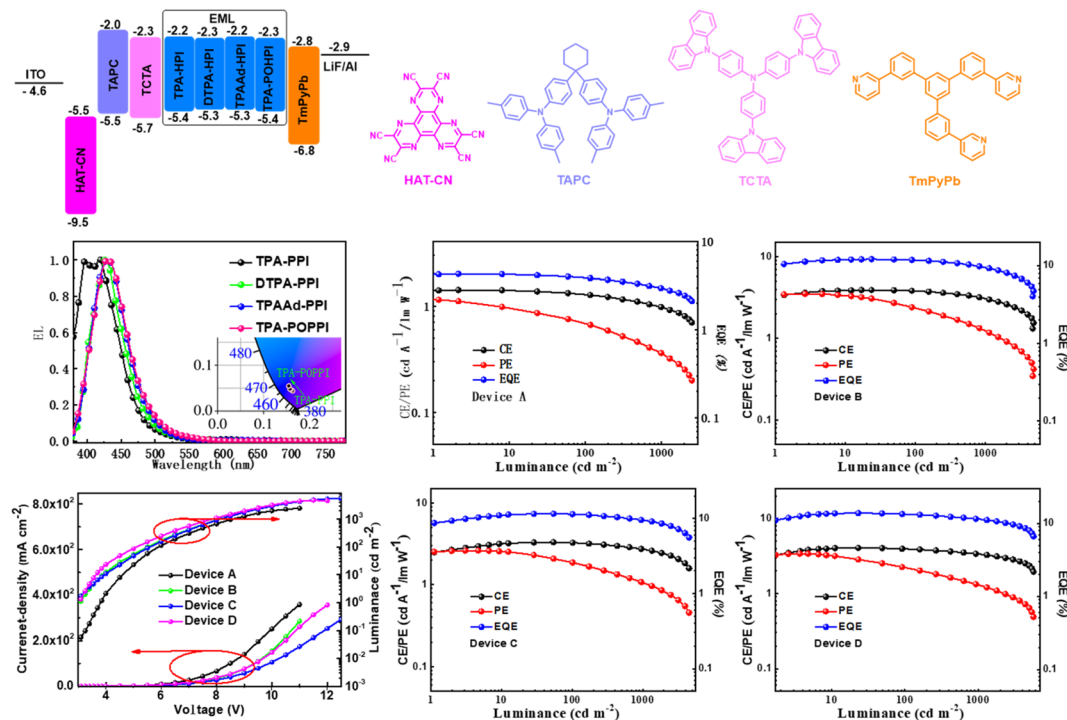
Fig. 5 Energy-level diagram and structure of the devices, chemical structure of the materials used in the OLEDs, voltage-dependent EL spectra of the devices based on TPA-PPI, DTPA-PPI, TPAAd-PPI and TPA-POPPI, current density–voltage–luminance (J–V–L) characteristics and relationship between EL efficiencies and luminance for the devices.

respectively (Fig. 5 and Table 1). The excellent EL properties indicate that HLCT materials have significant potential for developing high-efficiency OLEDs. Additionally, their radiative EUE (including singlet and triplet) ($\Phi_{S/T}$) is estimated according to the following formula:[30] $\mathrm{EQE} = \Phi_{PL} \times \gamma \times \Phi_{S/T} \times \eta_{out}$; where Φ_{PL} is the PLQY in the doped PMMA film of the emitters; γ is the electron–hole balance efficiency, which is supposed to be 100% in the ideal case; and η_{out} is the light-out-coupling efficiency that is generally assumed to be 20% for planar devices without

any light-out-coupling structures. The calculation results indicate that the EUE of TPA-PPI, DTPA-PPI, TPAAd-PPI and TPA-POPPI is 36.7%, 61.3%, 61.7% and 67.3%, respectively, whereas the theoretical upper limit for conventional fluorophores is only 25%. Therefore, the high EUE of these four emitters is expected to result from their HLCT character, which means the RISC from T_n ($n > 2$) to S_1 as a "hot exciton" channel is mainly responsible for the formation of a large proportion of singlet excitons, contributing to radiative emission. This also

Table 1 EL performance of PhSeDB and PhSeB based devices

Device	Emitter	$V_{turn-on}$ (V)	Luminance L_{max}^a (cd m^{-2})	EQE (%)	CE (cd A^{-1})	PE (lm W^{-1})	$\lambda_{max}{}^d$ (nm)	EUE^e (%)
A	TPA-PPI	3.0	2506.4 (11.0)	5.6 (4.0)^a 5.0^b 3.7^c	1.4 (4.0) 1.3 0.9	1.2 (3.4) 0.7 0.3	396, 420 (0.163, 0.044)	36.7
B	DTPA-PPI	3.1	4536.5 (11.0)	12.1 (4.0)^a 11.6^b 9.7^c	3.9 (4.0) 3.8 3.1	3.5 (3.5) 2.4 1.3	426 (0.159, 0.047)	61.3
C	TPAAd-PPI	3.1	4711.8 (12.0)	11.6 (5.0)^a 11.4^b 9.1^c	3.3 (5.0) 3.3 2.7	2.6 (3.2) 1.9 1.0	431 (0.157, 0.048)	61.7
D	TPA-POPPI	3.1	5687.7 (12.5)	13.8 (4.5)^a 13.1^b 11.1^c	4.0 (4.5) 3.9 3.4	3.4 (3.5) 2.3 1.3	431 (0.155, 0.054)	67.3

^{a} Maximal value of these devices. Values in the parentheses are the voltages at which they were obtained. ^{b} Values collected at 100 cd m^{-2}. ^{c} Values collected at 1000 cd m^{-2}. ^{d} Values are collected at 6 V for devices A–D and CIE coordinates (x, y) are shown in parentheses. ^{e} The exciton utilization efficiency for these four emitters.

confirms that confining the molecular transition to the PPI core and balancing the ratio of the CT and LE states are beneficial for enhancing the EUE of the material.

Additionally, TPAAd-PPI exhibits a significantly higher EQE compared to its main backbone analogue DPM (EQE, 4.0%).[31] In contrast to DPM, where the LUMO is primarily localized on the PPI unit, the LUMO of TPAAd-PPI is mainly distributed along the PPI main backbone. This suggests that directly incorporating diphenylamine into the side phenyl ring not only modulates the excited-state characteristics of the emitter but also enhances EUE, thereby substantially improving EL performance. At the luminance levels of 100 and 1000 cd m^{-2}, the EQE values remain 13.8% and 11.1% in the D device, which are superior to the EQE values of the other three devices. This can be attributed to the high and balanced hole/electron mobility of TPA-POPPI. The non-doped devices A, B, C and D exhibit stable NUV emission with the CIE coordinates of (0.163, 0.044), (0.159, 0.047), (0.157, 0.048) and (0.155, 0.054) (Fig. 5 and Table 1), and all EL spectra fall within the NUV region. These outstanding EL properties demonstrate that the molecular design strategy of separately introducing D and A groups on the side phenyl ring and main backbone of PPI can effectively modulate excited-state characteristics and balance charge carrier injection and transport, providing an effective molecular engineering solution for achieving high-performance NUV-OLEDs.

3 Conclusions

In summary, by directly introducing the electron-donating diphenylamine group into the side phenyl ring of PPI and further incorporating different donor or acceptor moieties into the main backbone to modulate the excited-state characteristics of the emitters, we successfully confined both the LE and CT states near the PPI core. This strategy enabled the design and synthesis of four high-performance hot-exciton NUV materials, denoted as TPA-PPI, DTPA-PPI, TPAAd-PPI, and TPA-POPP. All four emitters exhibit excellent thermal stability, enhanced PLQY, and well-balanced bipolar charge transport properties, while maintaining efficient ultraviolet emission and hRISC characteristics. Moreover, the non-doped device based on TPAAd-PPI achieved an outstanding external quantum efficiency (EQE) of 12.1%, significantly surpassing the 4.0% efficiency of the structurally similar DMP-based device. This result clearly demonstrates that direct incorporation of diphenylamine into the side phenyl ring effectively modulates the excited-state characteristics, thereby enhancing EL performance. Furthermore, the non-doped device employing TPA-POPPI attained a remarkable EQE of 13.8%, maintaining a stable efficiency of 11.1% even at a high brightness of 1000 cd m^{-2}. This study demonstrates the significant potential of molecular engineering strategies involving direct incorporation of electron-donating groups into the PPI side phenyl ring combined with further introduction of donor or acceptor moieties in the main backbone, representing an effective design approach for developing high performance NUV emitters and advanced OLED systems.

Author contributions

Daokun Zhong and Jie Zhang performed research; Daokun Zhong, Guijiang Zhou and Wai-Yeung Wong designed research; Ruiqin Zhu fabricated the device; Ling Yue provided computational support; Peng Tao, Bochao Su, Xiaolong Yang and Yuanhui Sun supervised the work; Daokun Zhong, Guijiang Zhou and Wai-Yeung Wong wrote the paper. All authors read and approved the final manuscript.

Conflicts of interest

There are no conflicts to declare.

Data availability

All relevant data are within the manuscript and its additional files.

Supplementary information is available. See DOI: **https://doi.org/10.1039/d5sc05477j**.

Acknowledgements

Notes and references

1 V. Jankus, C. J. Chiang, F. Dias and A. P. Monkman, *Adv. Mater.*, 2012, **25**, 1455–1459.

2 C. K. Moon, K. Suzuki, K. Shizu, C. Adachi, H. Kaji and J. J. Kim, *Adv. Mater.*, 2017, **29**, 1606448.

3 H. Uoyama, K. Goushi, K. Shizu, H. Nomura and C. Adachi, *Nature*, 2012, **492**, 234–238.

4 S. Ying, Y. Wu, Q. Sun, Y. Dai, D. Yang, X. Qiao, J. Chen and D. Ma, *Appl. Phys. Lett.*, 2019, **114**, 033501.

5 W. Li, D. Liu, F. Shen, D. Ma, Z. Wang, T. Feng, Y. Xu, B. Yang and Y. Ma, *Adv. Funct. Mater.*, 2012, **22**, 2797–2803.

6 J. Lv, S. Song, J. Li, L. Peng, Y. Li, Y. Liu, D. Ma, S. Ying and S. Yan, *Adv. Opt. Mater.*, 2023, **12**, 2301413.

7 T. T. Le, H. Nagata, A. Takahashi, M. Aihara, T. Okamoto, T. Shimohata, K. Mawatari, M. Akutagawa, Y. Kinouchi and M. Haraguchi, *J. Med. Investig.*, 2012, **59**, 53–58.

8 J. H. Lee, J. X. Huang, C. H. Chen, Y. T. Lee, C. Y. Chan, Y. C. D zeng, P. W. Tang, C. Chen, C. Adachi, T. L. Chiu, J. H. Lee and C. T. Chen, *Adv. Opt. Mater.*, 2023, **11**, 2202666.

9 S. Wang, R. Zhang, R. Ding, H. Huang, H. Qi, Y. Liu, S. Ying, D. Ma and S. Yan, *Chem. Sci.*, 2025, **16**, 5518–5527.
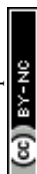
10 W. Qin, Z. Yang, Y. Jiang, J. W. Y. Lam, G. Liang, H. S. Kwok and B. Z. Tang, *Chem. Mater.*, 2015, **27**, 3892–3901.

11 H. Zhou, R. Wang, M. Sun, Y. Zhou, L. Zhang, J. Song, Q. Sun, S.-T. Zhang, W. Yang and S. Xue, *Chem. Sci.*, 2024, **15**, 18601–18607.

12 X. Lv, M. Sun, L. Xu, R. Wang, H. Zhou, Y. Pan, S. Zhang, Q. Sun, S. Xue and W. Yang, *Chem. Sci.*, 2020, **11**, 5058–5065.

13 G. Zhao, D. Liu, P. Wang, X. Huang, H. Chen, Y. Zhang, D. Zhang, W. Jiang, Y. Sun and L. Duan, *Angew. Chem., Int. Ed.*, 2022, **134**, e202212861.

14 L. Liang, C. Qu, X. Fan, K. Ye, Y. Zhang, Z. Zhang, L. Duan and Y. Wang, *Angew. Chem., Int. Ed.*, 2024, **63**, e202316710.

15 H. Wang, J. X. Chen, Y. Z. Shi, X. Zhang, L. Zhou, X. Y. Hao, J. Yu, K. Wang and X. H. Zhang, *Adv. Mater.*, 2023, **36**, 2307725.

16 T. Jairam and W. P. Hong, *J. Mater. Chem. C*, 2022, **10**, 16173–16217.

17 Q. Luo, Y. Gao, Y. Bai, M. Wu, H. Xu, H. Wang, D. Zheng and J. Yu, *Adv. Opt. Mater.*, 2024, **13**, 2402881.

18 X. Wang, Z. Liu, S. Geng, Z. Zhong, H. Li, X. J. Feng, Z. Zhao and H. Lu, *J. Mater. Chem. C*, 2023, **11**, 5316–5323.

19 S. Rana, S. R. Nayak, A. Saenubol, V. Promarak, S. Patel and S. Vaidyanathan, *Adv. Funct. Mater.*, 2025, 2507011.

20 S. Xiao, Y. Gao, R. Wang, H. Liu, W. Li, C. Zhou, S. Xue, S.-T. Zhang, B. Yang and Y. Ma, *Chem. Eng. J.*, 2022, **440**, 135911.

21 Z. Wang, P. Lu, S. Chen, Z. Gao, F. Shen, W. Zhang, Y. Xu, H. S. Kwok and Y. Ma, *J. Mater. Chem.*, 2011, **21**, 5451.

22 X. Tang, Q. Bai, Q. Peng, Y. Gao, J. Li, Y. Liu, L. Yao, P. Lu, B. Yang and Y. Ma, *Chem. Mater.*, 2015, **27**, 7050–7057.

23 W. Cui, C. Liu, X. Chao, M. Xie, Q. Sun, D. Liu, Y. Pan, S. T. Zhang and S. Xue, *Adv. Opt. Mater.*, 2023, **11**, 2202947.

24 J. D. Girase, Shahnawaz, J.-H. Jou, S. Patel and S. Vaidyanathan, *Dyes Pigm.*, 2022, **206**, 110623.

25 W. Li, P. Chasing, W. Benchaphanthawee, P. Nalaoh, T. Chawanpunyawat, C. Kaiyasuan, N. Kungwan, S. Namuangruk, T. Sudyoadsuk and V. Promarak, *J. Mater. Chem. C*, 2021, **9**, 497–507.

26 H. Zhou, R. Wang, S. T. Zhang, W. Cui, S. Ying, Q. Sun, B. Yang, S. Xue, W. Yang and Y. Ma, *Mater. Today Chem.*, 2022, **24**, 100785.

27 M. Sun, C. Ma, M. Xie, L. Chu, Q. Sun, W. Yang and S. Xue, *Chem. Eng. J.*, 2024, **480**, 148107.

28 P. Chasing, J. Kumsampao, P. Janthakit, P. Nalaoh, T. Loythaworn, W. Waengdongbung, P. Wongkaew, T. Sudyoadsuk and V. Promarak, *J. Mater. Chem. C*, 2023, **11**, 14776–14786.

29 S. Ge, C. Du, Z. Cheng, Y. Wang, Z. Feng, Z. Yan, Y. Hu and P. Lu, *Chem. Eng. J.*, 2024, **489**, 151314.

30 X. Chen, Z. Yang, W. Li, Z. Mao, J. Zhao, Y. Zhang, Y.-C. Wu, S. Jiao, Y. Liu and Z. Chi, *ACS Appl. Mater. Interfaces*, 2019, **11**, 39026–39034.

31 S. Xiao, S.-T. Zhang, Y. Gao, X. Yang, H. Liu, W. Li and B. Yang, *Dyes Pigm.*, 2021, **193**, 109482.